

A fundamental plane of black hole accretion at millimetre wavelengths

Ilaria Ruffa,^{1*} Timothy A. Davis,¹ Jacob S. Elford,¹ Martin Bureau,² Michele Cappellari,² Jindra Gensior,³ Daryl Haggard,⁴ Satoru Iguchi,^{5,6} Federico Lelli,⁷ Fu-Heng Liang,² Lijie Liu,^{8,9} Marc Sarzi,¹⁰ Thomas G. Williams,² and Hengyue Zhang²

¹Cardiff Hub for Astrophysics Research & Technology, School of Physics & Astronomy, Cardiff University, Queens Buildings, The Parade, Cardiff, CF24 3AA, UK

²Sub-department of Astrophysics, Department of Physics, University of Oxford, Keble Road, Oxford, OX1 3RH, UK

³Institute for Computational Science, University of Zurich, Winterthurerstrasse 190, Zürich, 8057, Switzerland

⁴Trottier Space Institute and Department of Physics, McGill University, 3600 rue University, Montreal, QC H3A 2T8, Canada

⁵Department of Astronomical Science, SOKENDAI (The Graduate University of Advanced Studies), Mitaka, Tokyo 181-8588, Japan

⁶National Astronomical Observatory of Japan, National Institutes of Natural Sciences, Mitaka, Tokyo 181-8588, Japan

⁷INAF, Arcetri Astrophysical Observatory, Largo Enrico Fermi 5, I-50125, Florence, Italy

⁸Cosmic Dawn Center (DAWN), Technical University of Denmark, DK2800 Kgs. Lyngby, Denmark

⁹DTU-Space, Technical University of Denmark, Elektrovej 327, DK2800 Kgs. Lyngby, Denmark

¹⁰Armagh Observatory and Planetarium, College Hill, Armagh BT61 9DG, UK

Accepted XXX. Received YYY; in original form ZZZ

ABSTRACT

We report the discovery of the “mm fundamental plane of black-hole accretion”, which is a tight correlation between the nuclear 1 mm luminosity ($L_{\nu, \text{mm}}$), the 2 – 10 keV X-ray luminosity ($L_{\text{X}, 2-10}$) and the supermassive black hole (SMBH) mass (M_{BH}) with an intrinsic scatter (σ_{int}) of 0.40 dex. The plane is found for a sample of 48 nearby galaxies, most of which are radiatively-inefficient, low-luminosity active galactic nuclei (LAGN). Combining these sources with a sample of high-luminosity (quasar-like) nearby AGN, we find that the plane still holds. We also find that M_{BH} correlates with $L_{\nu, \text{mm}}$ at a highly significant level, although such correlation is less tight than the mm fundamental plane ($\sigma_{\text{int}} = 0.51$ dex). Crucially, we show that spectral energy distribution (SED) models for both advection-dominated accretion flows (ADAFs) and compact jets can explain the existence of these relations, which are not reproduced by the standard torus-thin accretion disc models usually associated to quasar-like AGN. The ADAF models reproduces the observed relations somewhat better than those for compact jets, although neither provides a perfect fit. Our findings thus suggest that radiatively-inefficient accretion processes such as those in ADAFs or compact (and thus likely young) jets may play a key role in both low- and high-luminosity AGN. This mm fundamental plane also offers a new, rapid method to (indirectly) estimate SMBH masses.

Key words: galaxies: active – galaxies: nuclei – black hole physics – X-rays: galaxies – submillimetre: galaxies

1 INTRODUCTION

The many details of the processes driving and regulating the connection between the growth of central super-massive black holes (SMBHs, found to lie at the centre of almost every galaxy with a stellar mass $> 10^9 M_{\odot}$) and the evolution of their host galaxies (so-called “co-evolution”; e.g. Kormendy & Ho 2013) are still poorly understood (e.g. D’Onofrio et al. 2021). Understanding the physics of accretion onto SMBHs, determining if and how it changes in objects with different types of nuclear activity, as well as setting accurate constraints on fundamental SMBH properties such as its mass,

are all fundamental steps to take the next leaps forward in our comprehension of the SMBH-host galaxy interplay.

The so-called “fundamental plane of BH accretion” (hereafter FP) is an empirical correlation between the SMBH masses (M_{BH}), 5 GHz radio ($L_{5\text{GHz}}$) and 2 - 10 keV X-ray ($L_{\text{X}, 2-10}$) luminosities, which was initially reported by Merloni et al. (2003) and Falcke et al. (2004). The origin of the FP is still debated, but it is widely believed to carry information on the physics of SMBH accretion (see e.g. Gültekin et al. 2019a for a detailed discussion). However, the scatter around this correlation varies significantly depending on the sample and the method used to fit the plane, reaching values up to 0.88 dex (see e.g. Merloni et al. 2003; Gültekin et al. 2009; Plotkin et al. 2012; Saikia et al. 2015; Gültekin et al. 2019a, and references therein). Furthermore, the nature of the

* E-mail: ruffai@cardiff.ac.uk

radio emission in the sources following the FP is not yet well understood (potentially arising from compact jets or complex shock dynamics). All the above somehow limit the diagnostic power of the FP.

In this paper, we report the discovery of a fundamental plane at millimetre wavelengths, namely the existence of a tight correlation between the nuclear (i.e. $\ll 100$ pc) mm luminosities ($L_{\nu, \text{mm}}$), M_{BH} and $L_{\text{X}, 2-10}$, which appears to hold for both high- and low-luminosity AGN (within $z \lesssim 0.05$). We also present potential physical interpretations of such correlation, and discuss how this discovery may have profound implications for our understanding of the central engines of galaxies with many different types of nuclear activities.

2 PRIMARY SAMPLE AND DATA

Our sample was primarily drawn from the mm-Wave Interferometric Survey of Dark Object Masses (WISDOM) project, which has the main aim of exploiting high-resolution Atacama Large Millimeter/submillimeter Array (ALMA) CO data to dynamically estimate SMBH masses in a varied sample of galaxies (e.g. [Davis et al. 2017](#)). In this work, we included 31 WISDOM galaxies (Table A1) at $z \lesssim 0.03$, spanning a range of AGN bolometric luminosities ($L_{\text{bol}} = 10^{41} - 10^{46} \text{ erg s}^{-1}$) and mostly (but not exclusively) having very low rates of accretion onto their central SMBHs ($\dot{M} \lesssim 10^{-3} \dot{M}_{\text{Edd}}$; [Elford et al. 2023](#)). As such, most of these objects are classified as low-luminosity AGN (LLAGN; [Ho 2008](#)). To increase the statistics, we supplemented the 31 WISDOM galaxies with a further 17 objects (Table A1), selected from the literature to have dynamical SMBH mass estimates, existing high-resolution ALMA 1 mm observations and high-quality X-ray data. The majority of these are massive nearby ellipticals and span ranges of L_{bol} and \dot{M} similar to those of the WISDOM sources. Hereafter, we refer to the 31 WISDOM plus 17 literature sources as the *primary sample*.

The 1 mm luminosities of all the primary sample sources were derived from high-angular-resolution ALMA Band 6 continuum observations, taken between 2013 and 2021 as part of a large number of projects. All data were reduced using the Common Astronomy Software Applications (CASA) pipeline ([McMullin et al. 2007](#)), adopting a version appropriate for each dataset and a standard calibration strategy. For more details on the data reduction see [Davis et al. \(2022\)](#).

For each dataset, continuum images were produced by combining the continuum spectral windows (SPWs) and the line-free channels of the line SPW (when included) using the CASA task TCLEAN in multi-frequency synthesis (MFS) mode. The resulting continuum maps have synthesised beams ranging from $0''.042$ to $0''.723$, corresponding to $6 - 330$ pc at the distances of our sources (average spatial resolution ≈ 25 pc). For each source, the continuum flux density f_{mm} was measured from the innermost synthesised beam, coincident with the galaxy core. The mm luminosities were then estimated as $L_{\nu, \text{mm}} = 4\pi D_{\text{L}}^2 f_{\text{mm}} \nu_{\text{obs}}$, where D_{L} is the luminosity distance and ν_{obs} the observed frequency (between 231 and 239 GHz). As all the data were obtained with long-baseline configurations, large-scale dust emission is resolved out. We thus typically detect only a point-like source at each galaxy centre, arising from unresolved core emission. In a small number of galaxies (3/48), the continuum emission is

slightly resolved, increasing the uncertainties of our measurements. Removing these 3 objects, however, does not affect our results in any way. The obtained $L_{\nu, \text{mm}}$ are listed in Table A1.

The intrinsic (absorption-corrected) 2–10 keV luminosities ($L_{\text{X}, 2-10}$) of the primary sample sources were retrieved from the literature (see [Elford et al. 2023](#), for details). Eight of these galaxies have no X-ray data available (Table A1) and were thus not considered in the parts of the analysis where $L_{\text{X}, 2-10}$ was required. For the vast majority of the objects with X-ray data (33/40), the adopted $L_{\text{X}, 2-10}$ was derived from *Chandra* observations, thus including only nuclear emission from the unresolved AGN core. For most of the *Chandra*-observed objects (26/33), $L_{\text{X}, 2-10}$ was retrieved from the catalogue of [Bi et al. \(2020\)](#), see also Table A1).

Accurate, dynamically-determined SMBH masses (from stellar, ionised gas, molecular gas and/or maser kinematics) are available for a total of 31 sources in the primary sample (Table A1). For those galaxies without an existing direct measurement, we estimated M_{BH} using the $M_{\text{BH}} - \sigma_*$ relation of [van den Bosch \(2016\)](#), where σ_* is the stellar velocity dispersion within one effective radius. This was retrieved from the compilations of [van den Bosch \(2016\)](#) and [Cappellari et al. \(2013\)](#) when available, from the HyperLeda database otherwise (<http://leda.univ-lyon1.fr>). Crucially, although our primary sample is constructed based on data availability only (and is thus not meant to be complete in any statistical sense), the sample galaxies do span four orders of magnitude in SMBH mass.

3 THE MM FUNDAMENTAL PLANE

As illustrated in Fig. 1 (left panel), the SMBH masses of our primary sample galaxies strongly correlate with their $L_{\nu, \text{mm}}$. A power law was fitted to the observed trend, using the `LTS_LINEFIT` routine ([Cappellari et al. 2013](#)). This combines the least-trimmed-squares (LTS) robust regression technique ([Rousseeuw 1984](#)) with a least-squares fitting algorithm, and allows for intrinsic scatter and uncertainties in all coordinates. The resulting best-fitting power law is:

$$\log_{10} \left(\frac{M_{\text{BH}}}{M_{\odot}} \right) = (0.79 \pm 0.08) \left[\log_{10} \left(\frac{L_{\nu, \text{mm}}}{\text{erg s}^{-1}} \right) - 39 \right] + (8.2 \pm 0.1), \quad (1)$$

with an observed scatter (σ_{obs}) of 0.55 dex and an estimated intrinsic scatter (σ_{int}) of 0.51 ± 0.08 dex. When including $L_{\text{X}, 2-10}$, we discover the existence of a tighter correlation (Fig. 1, right panel). In this case, we used the `LTS_PLANEFIT` routine ([Cappellari et al. 2013](#)) to find the best-fitting plane in the $(\log M_{\text{BH}}, \log L_{\text{X}, 2-10}, \log L_{\nu, \text{mm}})$ space:

$$\begin{aligned} \log_{10} \left(\frac{M_{\text{BH}}}{M_{\odot}} \right) = & (-0.23 \pm 0.05) \left[\log_{10} \left(\frac{L_{\text{X}, 2-10}}{\text{erg s}^{-1}} \right) - 40 \right] \\ & + (0.95 \pm 0.07) \left[\log_{10} \left(\frac{L_{\nu, \text{mm}}}{\text{erg s}^{-1}} \right) - 39 \right] + (8.35 \pm 0.08), \end{aligned} \quad (2)$$

with $\sigma_{\text{obs}} = 0.45$ dex and $\sigma_{\text{int}} = 0.40 \pm 0.07$ dex. We verified that this multi-variate plane fit provides a significantly better predictor for the SMBH mass than the simple line fit, having a $\Delta_{\text{BIC}} >> 10$ (where Δ_{BIC} is the difference in the Bayesian information criterion between the line and plane fits). For

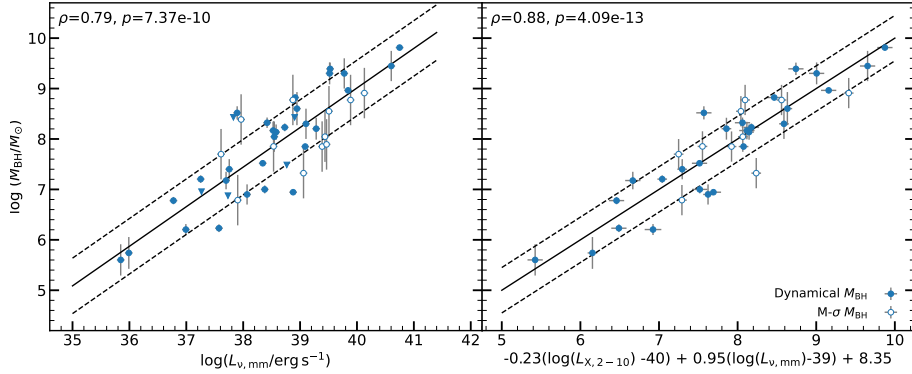


Figure 1. **Left panel:** Correlation between M_{BH} and $L_{\nu,\text{mm}}$ for the primary sample galaxies. **Right panel:** Edge-on view of the mmFP, showing the correlation between M_{BH} , $L_{\text{X},2-10}$, and $L_{\nu,\text{mm}}$ for the primary sample galaxies with all the three parameters available. In both panels, filled blue circles show sources with dynamical M_{BH} measurements, open circles sources with M_{BH} from the $M_{\text{BH}} - \sigma_*$ relation of van den Bosch (2016). Error bars are plotted for all points and all parameters but some are smaller than the symbol used. The best-fitting power-laws (Section 3) are overlaid as a black solid lines, the observed scatter as black dashed lines. The correlation coefficients ρ and p -values of the performed Spearman rank analysis are reported in the top-left corner of each panel.

both correlations, we also performed Spearman rank analyses to quantify their statistical significance, and show the resulting correlation coefficients in the top-left corner of each panel of Fig. 1. Since the mm and X-ray emission from AGN is known to be time variable (by a factor of typically 2–3 over year timescales; Prieto et al. 2016; Fernández-Ontiveros et al. 2019), variability likely dominates the scatters observed in Fig. 1 (and thus the underlying correlations may be even tighter). By analogy with the previous FP, we dub the correlation in the right panel of Fig. 1 as the “mm fundamental plane of BH accretion” (hereafter mmFP).

We note that the flux calibration uncertainty of the ALMA data introduces uncertainties in the derived $L_{\nu,\text{mm}}$. This is currently estimated to be $\approx 10\%$ in ALMA band 6. We included such uncertainty in the $L_{\nu,\text{mm}}$ error budget, but note that this is smaller than the estimated intrinsic scatters and thus likely to have a negligible impact on our results. We also note that the $L_{\text{X},2-10}$ of the five sample sources without available *Chandra* data could be slightly overestimated, due to contamination from diffuse hot gas in the galactic and circum-galactic medium (CGM; although this mainly emits in the 0.3–2 keV range) and/or X-ray binaries. While any such contamination should be minimal (based on the scaling laws of Grimm et al. 2003, Kim & Fabbiano 2004 and Boroson et al. 2011), we cannot rule it out entirely. In any case, removing these five sources does not make any relevant change in the parameters of the best-fitting mmFP reported above. The same applies when removing the sources in the primary sample without a dynamical M_{BH} estimate (the best-fitting line and planes are identical, within their respective errors, and the observed scatters become only slightly smaller).

3.1 BASS galaxies

Although the majority of the primary sample galaxies are LLAGN, a handful are more luminous systems (see Elford et al. 2023), which still follow the mmFP. To investigate whether this result holds more generally, we built a comparison sample from the *Swift*-BAT AGN Spectroscopic Survey (BASS), comprising AGN with median $z = 0.05$, $L_{\text{bol}} = 10^{44} \text{ erg s}^{-1}$ and $M = 0.01 - 0.1 \dot{M}_{\text{Edd}}$ (Koss et al. 2017).

We included in our analysis only the BASS sources for which both ALMA 1 mm observations (with spatial resolutions similar to those of the primary sample sources) and nuclear $L_{\text{X},2-10}$ were available (88 sources; Kawamuro et al. 2022). The SMBH masses of these objects were taken from the compilation of Koss et al. (2022). The BASS galaxies are typically more distant than those in the primary sample, so their M_{BH} have been estimated with a variety of methods (see Fig. B1). A small number of sources have dynamical M_{BH} measurements (9/88), while others have M_{BH} from reverberation mapping (13/88) or the widths of broad Balmer emission lines (16/88). For the remaining sources (50/88), M_{BH} is indirectly estimated using the $M_{\text{BH}} - \sigma_*$ relation of Kormendy & Ho (2013). We re-calibrated these measurements using the $M_{\text{BH}} - \sigma_*$ relation of van den Bosch (2016), for consistency with the 17 sources in the primary sample without a dynamical SMBH mass estimate.

As shown by Fig. 2b, the BASS sources are in agreement with the best-fitting mmFP, albeit with a larger observed scatter. We performed a Spearman rank analysis to quantify the statistical significance of this relation for the BASS points alone, and verified that they do show a significant correlation ($p = 0.002$), but with a correlation coefficient ($\rho = 0.32$) smaller than that of the primary sample. Fig. B1 suggests that the larger scatter in this population is at least partly driven by the M_{BH} uncertainties, as the position of a BASS galaxy with respect to the best-fitting mmFP depends on the method used to estimate its M_{BH} . For instance, sources with M_{BH} from reverberation mapping or broad-line methods are located systematically below the best-fitting line, likely reflecting the different biases in place when using such techniques (e.g. Farrah et al. 2023).

4 PHYSICAL DRIVERS

The fact that the BASS galaxies are consistent with a relation mainly defined by LLAGN is surprising. As discussed below, if (as expected) their nuclear mm continuum arises from accretion disc light reprocessed by dust in the torus, the BASS sources would be expected to fall off the observed

relation by at least two orders of magnitude. Our finding suggests that the dominant mechanism giving rise to the nuclear mm continuum (and its correlation with that producing the 2 – 10 keV emission) may be similar to the one in LLAGN. To determine the underlying physics, we compared the observed nuclear mm and X-ray luminosities of both the primary sample and BASS sources to those extracted from mock nuclear SEDs arising from radiatively-inefficient (ADAF-like) and “classic” (geometrically-thin and optically-thick) accretion flows, and from compact radio jets.

4.1 Torus model

AGN in the BASS sample (and a few galaxies in the primary sample) have *estimated* accretion rates in the range $\dot{M} \sim 0.01\text{--}0.1 \dot{M}_{\text{Edd}}$. According to the standard paradigm, in this type of systems the accretion should occur through the classic geometrically-thin and optically-thick accretion disc surrounded by a dusty torus (e.g. Heckman & Best 2014). In this scenario, both the mm and the 2 – 10 keV emission arise from the accretion disc, reprocessed by dust in the torus in the mm and Compton-up scattered by the hot corona in X-rays. To check if this type of model can explain the correlations in Fig. 1, we used SKIRTOR (Stalevski et al. 2012, 2016) – a library of emission models for classic AGN with dusty torii. The SED models were retrieved from the SKIRTOR webpage (<https://sites.google.com/site/skirtorus/>). The wavelength coverage of SKIRTOR (from 300 GHz to 1.24 keV) is slightly shorter than that required for this work. We thus expanded the models to the full range of wavelengths probed here, treating the emission mechanisms self-consistently as prescribed in the original version of the code (i.e. using the same grey-body curve for millimetre emission, and a power-law in the X-ray regime; Yang et al. 2020). We followed the prescriptions of Stalevski et al. (2012, 2016) to scale the models for different L_{bol} , in the range $10^{7.5} \text{--} 10^{12.5} L_{\odot}$ (i.e. the range covered by the primary and BASS sources; the torus is expected to disappear at low accretion rates, but the resulting model predictions are nevertheless instructive). For each SKIRTOR SED model, we then extracted the predicted 1 mm (specifically, the luminosity at 237.5 GHz, that is the median ALMA continuum frequency for both the primary and BASS sources) and intrinsic 2–10 keV luminosities, and compared them with the measured ones. The resulting predictions are shown in Fig. 2a as a hexagonally binned histogram (coloured by mean L_{bol}). The torus model reasonably reproduces the slope of the $L_{\text{X,2–10}} - L_{\nu,\text{mm}}$ relation of the BASS sources, but with an offset of about two orders of magnitude at a given L_{bol} . On the other hand, Fig. 2a shows that, to explain the mm luminosities of the lower accretion rate galaxies, the mm flux in the SKIRTOR models would need to be at least four orders of magnitude larger at a given accretion rate (and thus X-ray luminosity).

4.2 ADAF model

To build model SEDs arising from radiatively-inefficient accretion flows around SMBHs, we used the “LLAGN” model of Pesce et al. (2021), itself a development of previous models by Narayan & Yi 1995a and Mahadevan 1997). In typical LLAGN and some (low-accretion-rate) Seyferts, the classic

accretion disc is either absent or truncated at some inner radius (the transition usually happens beyond a few tens of Schwarzschild radii), and replaced by a geometrically-thick two-temperature structure in which the ion temperature is greater than the electron temperature and the accretion occurs at rates well below the Eddington limit (i.e. $\ll 0.01 \dot{M}_{\text{Edd}}$; Narayan & Yi 1995b; Ho 2008). The electrons in such radiatively-inefficient flows (such as advection-dominated accretion flows; ADAFs) cool down via a combination of self-absorbed synchrotron, bremsstrahlung and inverse Compton radiation, which together give rise to the nuclear SED from the mm to the X-rays. The LLAGN model adopted here solves for the energy balance between the heating and cooling of the electrons in the flow. We generated a set of model SEDs for a grid of SMBH masses ($10^6 \text{--} 10^{10} M_{\odot}$) and Eddington ratios ($10^{-7} \text{--} 10^{-2}$), while all the other free parameters were kept at the defaults discussed in Appendix A of Pesce et al. (2021). We then extracted the predicted 237.5 GHz and 2 – 10 keV luminosities, as described above. As illustrated by the shape of the model grid in Fig. 2a, the mm and X-ray luminosities of all the sources (and thus the observed correlations) are well explained if they arise from an ADAF-like accretion mechanism. The grid is almost aligned with the axes, thus predicting that the mm luminosity primarily depends on M_{BH} , while $L_{\text{X,2–10}}$ primarily traces the Eddington ratio. The tighter correlation obtained when including $L_{\text{X,2–10}}$ can be explained by the fact that the slight tilt of the grid is then taken into account, especially at higher Eddington ratios. A 3D version of Fig. 2a is provided as supplementary online material. In Fig. 2b, we show the projection of the ADAF model grid onto the best-fitting mmFP. This latter seems to arise naturally from these models, as an (almost) edge-on view of the 3D (M_{BH} , $L_{\text{X,2–10}}$, $L_{\nu,\text{mm}}$) relation. We note, however, that keeping the default model parameters from Pesce et al. (2021), the model well predicts the gradient of the mmFP, but is offset by a small amount (i.e. the model overpredicts $L_{\nu,\text{mm}}$ at a given SMBH mass by ≈ 0.5 dex). Tweaking the model parameters to reduce the effective radiative efficiency easily removes this offset (e.g. by changing some combination of the effective viscosity, ratio of gas to magnetic pressure, fraction of viscous heating going directly to the electrons, outer radius of the ADAF, and/or power-law index of the mass accretion rate as a function of radius). However, as the correct values of these parameters is not well constrained, here we simply offset the model grid by a constant 0.5 dex in SMBH mass to align it with the observed correlation. We stress that this scaling factor is significantly smaller than the one required for torus models to reproduce the observed trend (see Section 4.1), and is well within the uncertainties for the adopted model parameters (see Pesce et al. 2021). Future work exploring the parameters of ADAF-like models in sources with more extensive (sub-)mm coverage will allow to better understand the observed correlation, the small offset, and the physics of accretion onto these SMBHs. This is discussed further in Section 5.

4.3 Compact jet model

Unlike extended jets, where the synchrotron emission is optically-thin, compact radio jets have self-absorbed synchrotron spectra in the mm (similar to those from ADAFs). Compact jets have been argued to dominate the SEDs of

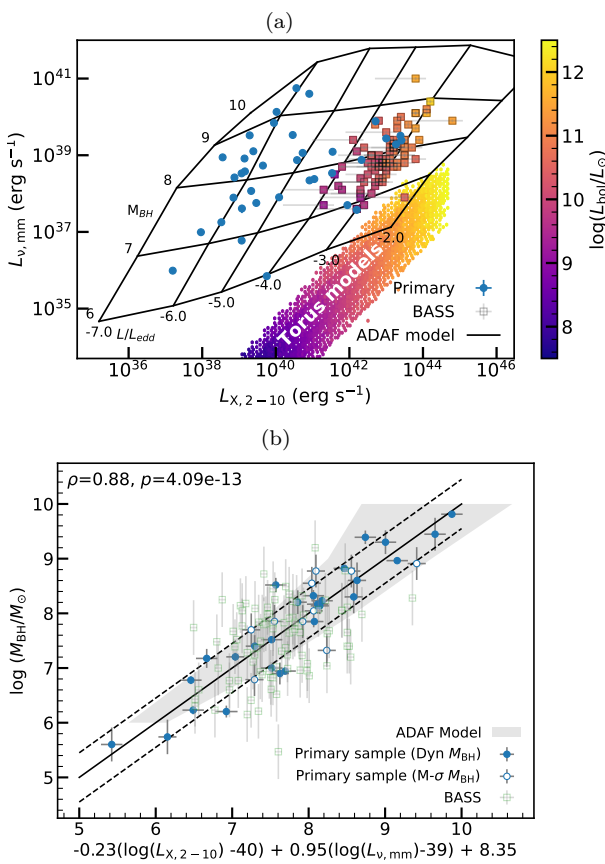


Figure 2. Top: Correlation between $L_{X,2-10}$ and $L_{\nu,\text{mm}}$ for the primary sample (blue circles) and the BASS (square symbols, coloured by their L_{bol}) sources. Error bars are plotted for all points and all parameters but some are smaller than the symbol used. The black grid illustrates the area covered by the ADAF model solutions as a function of M_{BH} and the Eddington ratio L/L_{Edd} (Section 4.2). The purple–yellow coloured bins indicate the region covered by the SKIRTOR torus models (Section 4.1), where each hexagonal bin is coloured by the mean L_{bol} of the sources within that bin. **Bottom:** As the right panel of Figure 1, but with the BASS galaxies overlaid as green squares and the grid of ADAF models from Figure 2a projected onto the plane as a grey shaded area (including a small offset for clarity; see Section 4.2).

LLAGN, and in some cases are preferred over a pure ADAF solution (as this would be overly luminous at near-infrared and optical wavelengths; e.g. Fernández-Ontiveros et al. 2023). To determine if compact jets can explain the trends observed in this work, we used the BHJET model of Lucchini et al. (2022). We fixed most of the model parameters to the values found for M81, a prototypical galaxy with compact jets (Model B in Table 3 of Lucchini et al. 2022), and generated a grid of models varying the SMBH mass (10^6 – $10^{10} M_{\odot}$), jet power ($10^{-5.5}$ – $10^{-0.5} L_{\text{Edd}}$) and jet inclination to the line-of-sight (2.5° – 90°). We then extracted from the resulting model SEDs the predicted $L_{\nu,\text{mm}}$ and $L_{X,2-10}$ (as above), and compare them with the estimated ones. In Fig. 3 we show the $L_{X,2-10}$ – $L_{\nu,\text{mm}}$ relation with the resulting model grids for the extremes in jet inclination (2.5° and 90°) overlaid. Jets at intermediate inclinations lie between these two extremes (but evolve quickly towards the $i=90^{\circ}$ solution once the line-of-sight is no longer aligned along the

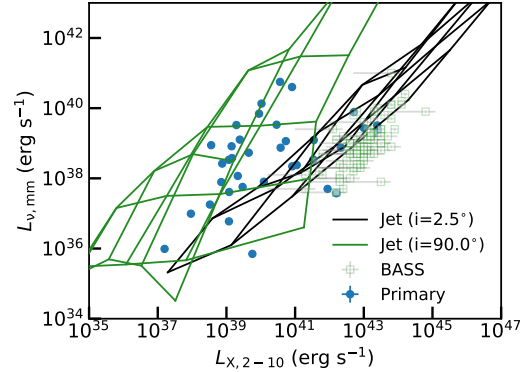


Figure 3. As Figure 2, but with slightly expanded axis ranges. In this case, the grids overlaid in black and green illustrate the areas covered by the compact jet model solutions as a function of M_{BH} and the jet power (Section 4.3), for jet inclinations of 2.5° and 90° , respectively. Solutions with intermediate inclinations lie in-between these two extremes.

jet cone). The model grids encompass the majority of the LLAGN and some BASS sources, but they are more complex than those of ADAFs, having significant curvature in the 3D $M_{\text{BH}}\text{--}L_{X,2-10}\text{--}L_{\nu,\text{mm}}$ space (a 3D version of Fig. 3 is provided as supplementary online material). The correlations in Fig. 1 do not seem to occur naturally within this model (as projections of the higher-order surface onto the axes). The luminosities of high-accretion-rate AGN from the primary and the BASS samples are harder to explain with these models, and would require additional X-ray emitting components. This is perhaps unsurprising, as compact jet models are substantially more complex than ADAFs (see also Section 5).

4.4 Distance uncertainties

Both SMBH mass and luminosity measurements are systematically affected by the assumed galaxy distance D , with $M_{\text{BH}} \propto D$ and $L \propto D^2$. Large distance errors can thus introduce large uncertainties on M_{BH} and L , and the difference in how these quantities scale with distance can give rise to spurious correlations. To test that this is not affecting our results, we performed a simple Monte Carlo simulation, drawing M_{BH} and the luminosities from independent Gaussian distributions that are truly uncorrelated, forcing a correlation to arise due to distance errors alone. The magnitude of the distance errors required to reproduce the Spearman rank correlation coefficients of the observed relations turned out to be very high (≥ 1.5 dex), much higher than that of our primary sample sources and – more in general – expected for real distance measurements. In addition, the slope of relations purely due to distance uncertainties would be substantially flatter than those observed (gradients of 0.5 for the $M_{\text{BH}}\text{--}L_{\nu,\text{mm}}$ correlation and 0.25 for the mmFP, as opposed to the observed ≈ 0.8 and ≈ 1 , respectively).

To further determine if any systematic distance bias could be affecting our results, we carried out a simple quality-checking exercise for our primary sample sources. We restricted our analysis to only those sources with the most accurate (redshift-independent) distances (26/48), i.e. derived from surface brightness fluctuations, tip of the red giant branch methods, supernovae, Cepheids, masers, the planetary nebula luminosity function and the globular cluster luminos-

ity function. This led us to obtain much tighter correlations, with an intrinsic scatter of 0.19 dex for the $M_{\text{BH}} - L_{\nu,\text{mm}}$ relation and only 0.11 dex for the mmFP. The corresponding Spearman rank coefficients are $\rho = 0.84$ ($p = 5.05 \times 10^{-7}$) and $\rho = 0.93$ ($p = 2.67 \times 10^{-9}$), respectively. We thus conclude that our results are not biased due to distance uncertainties.

5 DISCUSSION AND CONCLUSIONS

We report here the finding of tight $M_{\text{BH}} - L_{\nu,\text{mm}}$ and $M_{\text{BH}} - L_{\text{X},2-10} - L_{\nu,\text{mm}}$ correlations (Fig. 1). We dub the latter the “mm fundamental plane of BH accretion” and find it to hold for both low- (mostly WISDOM) and high- (mostly BASS) luminosity AGN. To understand the physics underlying the mmFP, we compared the observed trend with models predicting the emission from different nuclear mechanisms. We find that the results for both our sample and the BASS sources are best explained if their emission in the mm and X-rays primarily arises from an ADAF-like process, but cannot be explained by a classic torus model (see Fig. 2). This suggests that some kind of radiatively-inefficient accretion process may play a role in both low- and high-luminosity AGN, at least in the range of luminosities and accretion rates probed by the sources included in this work. While torii are known to exist in many of these AGN, some regions around their SMBHs may be radiatively-inefficient. For instance, some accretion disc solutions allow discs to transition from ADAF-like to geometrically-thin, and vice versa at different radii (Mahadevan 1997). ADAFs could also exist above and below classic accretion discs (Mahadevan 1997). Although the exact conditions under which this applies are still to be investigated, it is clear that - if confirmed - our results will have profound implications for our understanding of the central engines of many different types of AGN.

We also explored the possibility that both the mm and the X-ray emission arise from compact (and thus likely young; O’Dea & Saikia 2020) radio jets (Section 4.3). These have been argued to dominate the whole SEDs of LLAGN (e.g. Fernández-Ontiveros et al. 2023) and have spectral properties similar to those of an ADAF at the wavelengths probed here. This is also consistent with one of the most popular scenarios for the origin of the radio FP of LLAGN, suggesting that the correlation arises from strongly sub-Eddington jet-dominated emission (e.g. Falcke et al. 2004; Plotkin et al. 2012). The contribution of compact radio jets to the nuclear SEDs of radiatively-efficient, quasar-like AGN is instead still hotly debated (e.g. Fawcett et al. 2020; Girdhar et al. 2022). Our results are marginally consistent with these scenarios, as we find that compact jet models can explain the correlations for most of the LLAGN, but additional X-ray emitting components are required in the higher-luminosity systems.

In short, we demonstrated that ADAF-like models convincingly predict the mmFP, which is not reproduced by a torus model. Compact jets are also an alternative plausible explanation (at least for LLAGN), but the corresponding models do not reproduce the correlation as naturally as the ADAF-like ones. We caution, however, that the plasma physics underlying both the ADAF and compact jet models is not well characterised, and significant uncertainties are present in all the model parameters and how they interact. We thus conclude that, while “classic” torus models seem to

be ruled out, either ADAFs or compact jets have the potential to explain the observed trend. The presence of one (or more) of these mechanisms could even help explaining the increased far-infrared/sub-mm contribution attributed to AGN in some empirical SED models (e.g. Symeonidis 2022). The tight $L_{\text{X},2-10} - L_{\nu,\text{mm}}$ correlation observed in Fig. 2a for the BASS sources is also consistent with the one recently reported by Ricci et al. (2023) between the 100 GHz mm and 14-150 keV X-ray luminosities, and our results add interesting clues onto its origin. Determining with certainty the relevant mechanism(s) giving rise to the observed correlations is beyond the scope of this work, but is crucial to further our understanding of the SMBH accretion/ejection processes in different types of AGN.

Beyond carrying information on the nuclear physics, the correlations presented here provide new rapid methods to indirectly estimate the mass of SMBHs (or their accretion rates, if one has alternative, robust estimates of M_{BH} and $L_{\nu,\text{mm}}$; see e.g. Ricci et al. 2023). Although direct M_{BH} estimates can be obtained using a variety of techniques (e.g. stellar or gas kinematics, reverberation mapping), these typically require very time-consuming observational campaigns and currently have limited application beyond the local Universe. The ability to use nuclear mm and (optionally) X-ray luminosities has the huge advantage of allowing M_{BH} estimates when dynamical measurements are not possible and/or the standard scaling relations are unusable (such as in dwarf or disturbed galaxies). It also allows SMBH mass predictions over a wider range of redshifts. At the high-mass end of the reported correlations, ALMA can allow us to constrain M_{BH} up to $z \approx 0.3$ (and is limited more by angular resolution and frequency coverage than sensitivity). Proposed new interferometers (such as the next-generation Very Large Array, ngVLA) should be able to push this to $z = 1$ and beyond. Large X-ray surveys that can provide complementary X-ray data are also ongoing (e.g. eROSITA), and next-generation satellites (such as the Advanced Telescope for High ENergy Astrophysics, *Athena*) will extend these to higher- z . We also note that the intrinsic scatter of the overall $M_{\text{BH}} - L_{\nu,\text{mm}}$ relation is comparable to that of the $M_{\text{BH}} - \sigma_*$ relation (e.g. van den Bosch 2016), and σ_{int} of the mmFP in Fig. 1 is comparable or even lower than that of its radio counterpart (depending on the sample used to fit the plane; see e.g. Merloni et al. 2003; Falcke et al. 2004; Gültekin et al. 2009; Plotkin et al. 2012; Gültekin et al. 2019b). When restricting our analysis to only those primary sample sources with the most accurate (redshift-independent) distances, we obtain much tighter correlations (see Section 4.4), with σ_{int} comparable to that of some of the tightest scaling relations in Astronomy (such as the Baryonic Tully-Fisher relation; e.g. Lelli et al. 2016, 2019). This technique - if sufficiently verified - is thus well suited to constrain the details of SMBH-host galaxy co-evolution in regimes that have been difficult to access up to now (Williams et al. 2023).

ACKNOWLEDGEMENTS

IR and TAD acknowledge support from grant ST/S00033X/1 through the UK Science and Technology Facilities Council (STFC). MB and TGW were supported by STFC consolidated grant ‘Astrophysics at Oxford’ ST/H002456/1 and ST/K00106X/1. DH acknowledges support from the Canada

Research Chairs (CRC) program, the NSERC Discovery Grant program, and the Canadian Tri-Agency New Frontiers in Research – Explorations fund. This paper makes use of ALMA data. ALMA is a partnership of ESO (representing its member states), NSF (USA) and NINS (Japan), together with NRC (Canada), NSC and ASIAA (Taiwan), and KASI (Republic of Korea), in cooperation with the Republic of Chile. The Joint ALMA Observatory is operated by ESO, AUI/NRAO and NAOJ. The National Radio Astronomy Observatory is a facility of the National Science Foundation operated under cooperative agreement by Associated Universities, Inc. This paper has also made use of the NASA/IPAC Extragalactic Database (NED) which is operated by the Jet Propulsion Laboratory, California Institute of Technology under contract with NASA. We acknowledge also the usage of the HyperLeda database.

DATA AVAILABILITY

The ALMA data used in this article are all available to download at the ALMA archive (<https://almascience.nrao.edu/asax/>). The calibrated data, final products and original plots generated for this research study will be shared upon reasonable request to the first author. The X-ray data have been retrieved from the catalogue of Bi et al. (2020) or from the NASA/IPAC Extragalactic Database (NED; <https://ned.ipac.caltech.edu/>). The routines, codes and libraries of emission models used to fit the correlations and obtain the model SEDs are all publicly available at the following links: LLAGNSED at <https://github.com/dpesce/LLAGNSED>, LTS_LINEFIT and LTS_PLANEFIT at <https://www-astro.physics.ox.ac.uk/~cappellari/software/#lts>, SKIRTOR at <https://sites.google.com/site/skirtorus/home>.

REFERENCES

Bi S., Feng H., Ho L. C., 2020, *ApJ*, **900**, 124
 Boroson B., Kim D.-W., Fabbiano G., 2011, *ApJ*, **729**, 12
 Cappellari M., et al., 2013, *MNRAS*, **432**, 1709
 D’Onofrio M., Marziani P., Chiosi C., 2021, *Frontiers in Astronomy and Space Sciences*, **8**, 157
 Davis T. A., Bureau M., Onishi K., Cappellari M., Iguchi S., Sarzi M., 2017, *MNRAS*, **468**, 4675
 Davis T. A., et al., 2022, *MNRAS*, **512**, 1522
 Elford J. S., et al., 2023, WISDOM Project - XVI. The link between circumnuclear molecular gas reservoirs and active galactic nucleus fuelling, Submitted to MNRAS
 Falcke H., Körding E., Markoff S., 2004, *A&A*, **414**, 895
 Farrah D., et al., 2023, *ApJ*, **943**, 133
 Fawcett V. A., Alexander D. M., Rosario D. J., Klindt L., Fotopoulos S., Lusso E., Morabito L. K., Calistro Rivera G., 2020, *MNRAS*, **494**, 4802
 Fernández-Ontiveros J. A., López-Gonzaga N., Prieto M. A., Acosta-Pulido J. A., Lopez-Rodriguez E., Asmus D., Tristram K. R. W., 2019, *MNRAS*, **485**, 5377
 Fernández-Ontiveros J. A., López-López X., Prieto A., 2023, *A&A*, **670**, A22
 Girdhar A., et al., 2022, *MNRAS*, **512**, 1608
 Grimm H. J., Gilfanov M., Sunyaev R., 2003, *MNRAS*, **339**, 793
 Gültekin K., et al., 2009, *ApJ*, **698**, 198
 Gültekin K., King A. L., Cackett E. M., Nyland K., Miller J. M., Di Matteo T., Markoff S., Rupen M. P., 2019a, *ApJ*, **871**, 80

Di Matteo T., Markoff S., Rupen M. P., 2019b, *ApJ*, **871**, 80
 Heckman T. M., Best P. N., 2014, *ARA&A*, **52**, 589
 Ho L. C., 2008, *ARA&A*, **46**, 475
 Kawamuro T., et al., 2022, *ApJ*, **938**, 87
 Kim D.-W., Fabbiano G., 2004, *ApJ*, **611**, 846
 Kormendy J., Ho L. C., 2013, *ARA&A*, **51**, 511
 Koss M., et al., 2017, *ApJ*, **850**, 74
 Koss M. J., et al., 2022, *ApJS*, **261**, 2
 Lelli F., McGaugh S. S., Schombert J. M., 2016, *ApJ*, **816**, L14
 Lelli F., McGaugh S. S., Schombert J. M., Desmond H., Katz H., 2019, *MNRAS*, **484**, 3267
 Lucchini M., et al., 2022, *MNRAS*, **517**, 5853
 Mahadevan R., 1997, *ApJ*, **477**, 585
 McMullin J. P., Waters B., Schiebel D., Young W., Golap K., 2007, in Shaw R. A., Hill F., Bell D. J., eds, Astronomical Society of the Pacific Conference Series Vol. 376, Astronomical Data Analysis Software and Systems XVI. p. 127
 Merloni A., Heinz S., di Matteo T., 2003, *MNRAS*, **345**, 1057
 Narayan R., Yi I., 1995a, *ApJ*, **444**, 231
 Narayan R., Yi I., 1995b, *ApJ*, **452**, 710
 O’Dea C. P., Saikia D. J., 2020, arXiv e-prints, p. arXiv:2009.02750
 Pesce D. W., et al., 2021, *ApJ*, **923**, 260
 Plotkin R. M., Markoff S., Kelly B. C., Körding E., Anderson S. F., 2012, *MNRAS*, **419**, 267
 Prieto M. A., Fernández-Ontiveros J. A., Markoff S., Espada D., González-Martín O., 2016, *MNRAS*, **457**, 3801
 Ricci C., et al., 2023, arXiv e-prints, p. arXiv:2306.04679
 Rousseeuw P. J., 1984, *Journal of the American Statistical Association*, **79**
 Saikia P., Körding E., Falcke H., 2015, *MNRAS*, **450**, 2317
 Stalevski M., Fritz J., Baes M., Nakos T., Popović L. Č., 2012, *MNRAS*, **420**, 2756
 Stalevski M., Ricci C., Ueda Y., Lira P., Fritz J., Baes M., 2016, *MNRAS*, **458**, 2288
 Symeonidis M., 2022, *MNRAS*, **509**, 3209
 Williams J. K., Gliozzi M., Bockwoldt K. A., Shuvo O. I., 2023, *MNRAS*, **521**, 2897
 Yang G., et al., 2020, *MNRAS*, **491**, 740
 van den Bosch R. C. E., 2016, *ApJ*, **831**, 134

APPENDIX A: DATA TABLE

APPENDIX B: THE SCATTER OF THE MM FP

We show here the residuals of our primary sample and BASS sources from the best-fitting mmFP, plotted as a function of the SMBH mass measurement method. This is important to get insights into the scatter of the two populations around the correlation (see Section 3.1 for details).

This paper has been typeset from a *TeX/LaTeX* file prepared by the author.

Table A1. Full list and main parameters of the galaxies in the primary sample.

Sample	Galaxy	D (Mpc)	$\log M_{\text{BH}}$ (M_{\odot})	$\Delta \log M_{\text{BH}}$ (dex)	Method	$\log L_{\nu, \text{mm}}$ (erg s^{-1})	$\log L_{\text{X}, 2-10}$ (erg s^{-1})	$\Delta \log L_{\text{X}, 2-10}$ (dex)
(1)	(2)	(3)	(4)	(5)	(6)	(7)	(8)	(9)
WISDOM	FRL49	85.7	8.20	0.2	Dyn	39.28	43.27	0.04
	FRL1146	136.7	7.85	0.30	σ_{\star}	< 38.76	43.41	0.04
	MRK567	140.6	7.48	0.30	σ_{\star}	39.39	—	—
	NGC0404	3.0	5.74	0.30	Dyn	35.99	37.20	0.04
	NGC0449	66.3	8.77	0.30	σ_{\star}	38.87	40.58	0.04
	NGC0524	23.3	8.60	0.32	Dyn	38.94	38.55	0.04
	NGC0708	58.3	8.30	0.30	Dyn	39.10	39.39	0.04
	NGC1194	53.2	7.85	0.10	Dyn	39.09	41.54	0.04
	NGC1387	19.9	6.90	0.20	Dyn	38.07	39.33	0.04
	NGC1574	19.3	8.05	0.20	Dyn	38.55	—	—
	NGC2110	35.6	8.77	0.30	σ_{\star}	39.89	42.71	0.04
	NGC3169	18.7	7.85	0.30	σ_{\star}	38.53	41.53	0.04
	NGC3351	10.0	5.85	0.30	σ_{\star}	< 37.25	38.74	0.04
	NGC3368	18.0	6.87	0.10	Dyn	< 37.73	39.30	0.05
	NGC3607	22.2	8.14	0.15	Dyn	38.58	39.16	0.04
	NGC4061	94.1	9.30	0.30	Dyn	39.78	—	—
	NGC4429	16.5	8.17	0.10	Dyn	38.08	39.12	0.10
	NGC4435	16.5	7.40	0.20	Dyn	37.76	39.47	0.04
	NGC4438	16.5	7.70	0.30	σ_{\star}	37.61	39.08	0.04
	NGC4501	14.0	6.79	0.30	σ_{\star}	37.90	40.0.9	0.04
	NGC4697	11.4	7.20	0.10	Dyn	37.25	38.52	0.04
	NGC4826	7.4	6.20	0.11	Dyn	36.99	37.96	0.11
	NGC5064	34.0	8.39	0.30	σ_{\star}	37.96	—	—
	NGC5765b	114.0	7.32	0.30	σ_{\star}	39.06	40.73	0.05
	NGC5806	21.4	6.95	0.30	σ_{\star}	< 37.26	—	—
	NGC5995	107.5	8.55	0.30	σ_{\star}	39.51	43.39	0.04
	NGC6753	42.0	8.42	0.30	σ_{\star}	< 37.82	—	—
	NGC6958	30.6	7.89	0.30	σ_{\star}	39.47	—	—
	NGC7052	51.6	8.91	0.30	σ_{\star}	40.13	40.02	0.05
	NGC7172	33.9	8.05	0.30	σ_{\star}	39.44	43.00	0.05
	PGC043387	95.8	8.42	0.30	σ_{\star}	38.90	—	—
Literature	Circinus	4.2	6.23	0.08	Dyn	37.57	42.20	0.04
	IC1459	25.9	9.45	0.30	Dyn	40.60	40.91	0.10
	M87	16.5	9.81	0.04	Dyn	40.75	40.56	0.05
	NGC1316	19.9	8.23	0.08	Dyn	38.73	39.65	0.04
	NGC1332	22.3	8.82	0.04	Dyn	38.91	39.15	0.08
	NGC1380	17.1	8.17	0.17	Dyn	38.53	39.07	0.04
	NGC3227	17.0	7.18	0.17	Dyn	37.70	41.95	0.09
	NGC3245	21.5	8.32	0.10	Dyn	38.42	38.88	0.09
	NGC3393	53.6	7.52	0.03	Dyn	38.34	40.92	0.09
	NGC3489	12.0	6.78	0.07	Dyn	36.77	39.07	0.09
	NGC3504	13.6	7.00	0.07	Dyn	38.38	41.05	0.09
	NGC3585	20.6	8.52	0.13	Dyn	37.89	38.85	0.04
	NGC4374	18.5	8.96	0.05	Dyn	39.84	39.95	0.04
	NGC4388	19.8	6.94	0.01	Dyn	38.88	42.33	0.05
	NGC4395	4.4	5.60	0.31	Dyn	35.85	39.91	0.05
	NGC6861	27.3	9.30	0.22	Dyn	39.52	39.29	0.04
	UGC2698	91.0	9.39	0.12	Dyn	39.53	40.46	0.09

Notes: (1) Sub-sample. (2) Galaxy name. (3) Most accurate galaxy distance. (4), (5) and (6) SMBH mass, uncertainty, and measurement method. “Dyn” refers to dynamical measurements, “ σ_{\star} ” to estimates from the $M_{\text{BH}} - \sigma_{\star}$ relation of [van den Bosch \(2016\)](#). (7) Millimetre luminosity. Errors are not reported because they are simply dominated by flux calibration uncertainties, which are $\approx 10\%$ for ALMA Band 6 (see Section 2). (8) and (9) 2 – 10 keV X-ray luminosity, and associated error. Galaxies highlighted in bold have their X-ray luminosity taken from the catalogue of [Bi et al. \(2020\)](#).

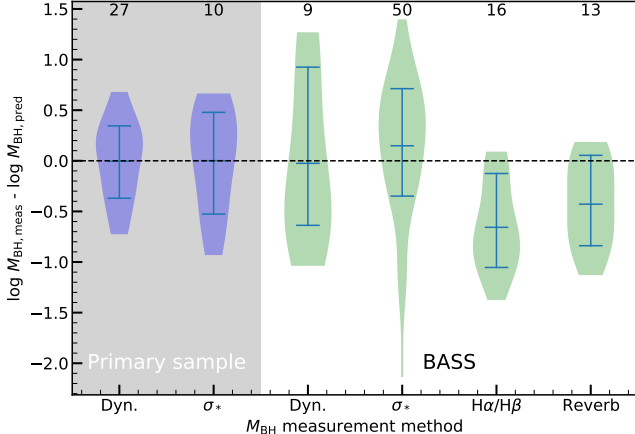


Figure B1. Residuals of our primary sample (grey shaded region) and BASS sources (white region) from the best-fitting mmFP, plotted as a function of the SMBH mass measurement method. “Dyn” refers to dynamical mass measurements, “ σ_* ” to estimates from the $M_{\text{BH}} - \sigma_*$ relation of [van den Bosch \(2016\)](#), “H α /H β ” to the broad-line method and “Reverb” to reverberation mapping. Each set of data points is represented by a violin describing the underlying distribution, shaded in blue for our primary sample and in green for the BASS sources. The numbers above each violin indicate the number of sources in the mmFP whose M_{BH} has been estimated using that particular method. In each case, the blue horizontal lines denote the 18th, 50th and 85th percentiles of the distribution.